A. Xu
Department of Mechanical and Aerospace Engineering,
HKUST Energy Institute,
The Hong Kong University of Science and Technology,
Hong Kong 999077, China

T. S. Zhao[1]
Fellow ASME
Department of Mechanical and Aerospace Engineering,
HKUST Energy Institute,
The Hong Kong University of Science and Technology,
Hong Kong 999077, China
e-mail: metzhao@ust.hk

L. Shi
Department of Mechanical and Aerospace Engineering,
HKUST Energy Institute,
The Hong Kong University of Science and Technology,
Hong Kong 999077, China

J. B. Xu
Department of Mechanical and Aerospace Engineering,
HKUST Energy Institute,
The Hong Kong University of Science and Technology,
Hong Kong 999077, China

Lattice Boltzmann Simulation of Mass Transfer Coefficients for Chemically Reactive Flows in Porous Media

We present lattice Boltzmann (LB) simulations for the mass transfer coefficient from bulk flows to pore surfaces in chemically reactive flows for both ordered and disordered porous structures. The ordered porous structure under consideration consists of cylinders in a staggered arrangement and in a line arrangement, while the disordered one is composed of randomly placed cylinders. Results show that the ordered porous structure of staggered cylinders exhibits a larger mass transfer coefficient than ordered porous structure of inline cylinders does. It is also found that in the disordered porous structures, the Sherwood number (Sh) increases linearly with Reynolds number (Re) at the creeping flow regime; the Sh and Re exhibit a one-half power law dependence at the inertial flow regime. Meanwhile, for Schmidt number (Sc) between 1 and 10, the Sh is proportional to $Sc^{0.8}$; for Sc between 10 and 100, the Sh is proportional to $Sc^{0.3}$.
[DOI: 10.1115/1.4038555]

1 Introduction

Transport phenomena in porous media are of considerable interest because of their wide application in engineering and natural processes. For example, the coupled electrolyte flows, heat and mass transfer, ions transport, and electrons transport in the porous electrode play a critical role in fuel cells and flow batteries [1,2]. Transport properties of the porous media, such as permeability, effective thermal conductivity, heat transfer coefficient, effective mass diffusivity, and mass transfer coefficient, are of practical interest to quantify the complex transport behaviors in porous media, further enabling the design and manufacture of porous structure that can meet specified requirements. Moreover, accurate transport properties are essential ingredients to formulate macroscopic mathematical models to gain insight into the physical–chemical process in porous media efficiently.

The approaches to obtain transport properties can be generally classified into three categories. The first category is theoretical analysis, including volume averaging method and multiscale asymptotics method [3,4]. The underlying idea of these methods is to define macroscale variables through homogenization. However, the applications of these methods are usually limited to ordered porous structure with periodical boundary condition, and the extension to complex disordered porous structure is rather difficult. The second category is experimental measurement, which can be used to obtain the transport properties accurately for specified samples [5,6]. However, as the pore geometry is rather complex involving many interacting geometric parameters, the information provided by experiments is usually insufficient to derive a general interpretation of the pore geometry effects upon transport properties. The third category is numerical simulation, which is not restricted by the geometrical structure of porous media, and can also provide detailed information on the transport process [7,8]. With the rapid increasing of computing capabilities, the numerical simulation is expected to play a more important role in the research of transport phenomena.

Previous efforts to obtain transport properties via numerical simulations have focused on calculating permeability [9,10], effective thermal conductivity [11,12], heat transfer coefficient [13–16], and effective mass diffusivity [17,18]. To our best knowledge, predicting the mass transfer coefficient, which can be used to quantify mass transfer from the bulk flow to pore surfaces [5], has rarely been reported. Generally, the mass transfer coefficient k_m can be defined as $k_m = N/(c_{\text{bulk}} - c_{\text{wall}})$, where N is the mass flux at the reactive wall surfaces, c_{bulk} and c_{wall} are the concentrations in the bulk solution and at the reactive wall surfaces, respectively. The dimensionless Sherwood number (Sh) is usually adopted to represent the mass transfer coefficient, and it is related to the geometry of porous media, fluid properties, and local velocity of the fluids. It is worth mentioning that a heat transfer correlation can be used in analogy to a mass transfer correlation by replacing the Nusselt number (Nu) with Sherwood number and replacing the Prandtl number (Pr) with Schmidt number (Sc); moreover, heat transfer correlations are easier to be determined from experimental work. Thus, heat transfer correlation received more attention in previous literatures. For example, Grucelski and Pozorski [19] considered heat transfer in a random arrangement of

[1]Corresponding author.

Contributed by the Heat Transfer Division of ASME for publication in the Journal of Heat Transfer. Manuscript received December 23, 2016; final manuscript received October 17, 2017; published online January 23, 2018. Editor: Portonovo S. Ayyaswamy.

circular cylinders and proposed the empirical correlation $Nu \propto Re^{0.6}Pr^{1/3}$ based on their direct numerical simulation data. On the other hand, Gamrat et al. [20] show that the constant wall temperature boundary condition and the constant volumetric heat source boundary condition have different effects on the heat transfer processes; then it is instinct to conjecture that the chemically reactive boundary condition will also influence the mass transfer process differently.

In this work, we present lattice Boltzmann (LB) simulations to predict mass transfer coefficient in chemically reactive flows. Among available numerical simulation techniques, the LB method has proved to be a promising tool for simulating fluid systems involving complex boundaries, primarily because the solid–fluid interface can be easily implemented by modifications on the distribution function encountering the interface [8]. The physical–chemical processes under investigation involve fluid flows, mass transfer, and heterogeneous chemical reaction.

2 Numerical Method

2.1 Mathematical Model for Fluid Flows, Mass Transfer and Heterogeneous Chemical Reaction. Fluid flows and associate transport processes in porous media can be described at different length scales, namely the representative elementary volume-scale and the pore-scale [8]. In this work, we consider the dominant processes at the pore-scale so that individual pore space is directly resolved. The governing equation for fluid flows in the pore space is the incompressible Navier–Stokes equations, which can be written as

$$\nabla \cdot \mathbf{u} = 0 \tag{1a}$$

$$\frac{\partial \mathbf{u}}{\partial t} + \mathbf{u} \cdot \nabla \mathbf{u} = -\frac{1}{\rho}\nabla p + \nu \nabla^2 \mathbf{u} \tag{1b}$$

where $\mathbf{u}$ and p are the local fluid velocity and pressure, respectively. In pore-scale approach, the effect of porous media is reflected through the incorporating of solid porous matrix with complex geometry in the computational domain. This treatment is opposite to that in representative elementary volume-scale approach, where the effect of porous media is reflected through the homogenization of governing equation [21,22].

The concentration for a dilute chemical species can be assumed as a passive scalar; then mass transfer in the pore space is described by the convection–diffusion equation, which is written as

$$\frac{\partial C}{\partial t} + \nabla \cdot (C\mathbf{u}) = \nabla \cdot (D \nabla C) \tag{2}$$

where C is the local solute concentration.

Heterogeneous reactions at solid–fluid interface are represented by

$$-D\frac{\partial C_w}{\partial n} = k_r (C_{\text{eq}} - C_w)^{\alpha} \tag{3}$$

Here, $\mathbf{n}$ denotes the unit normal vector at the solid wall pointing to the fluid region, as shown in Fig. 1. k_r is the reaction-rate constant, C_{eq} is equilibrium concentration, and α is the order of reaction kinetics. In the present work, we only consider first-order chemical reaction, namely $\alpha = 1$. Choosing the dimensionless scale for concentration as $C^* = C/C_{\text{eq}}$, and introducing Damköhler number (Da) to represent the ratio of reaction rate to mass transfer rate $\text{Da} = k_r/(D/L)$, where L is characteristics length, then Eq. (3) can be rewritten as

$$\frac{\partial C_w^*}{\partial n} = \frac{\text{Da}}{L}\left(C_w^* - 1\right) \tag{4}$$

2.2 Lattice Boltzmann Model for Fluid Flows and Mass Transfer. In LB method, the most popular collision model is lattice Bhatnagar–Gross–Krook (LBGK) model [23] with single-relaxation-time approximation for the complex collision operator. However, it has been reported by Pan et al. [9] that LBGK model would result in viscosity dependence of boundary locations; thus, the prediction of permeability in porous media depends on relaxation parameters. Similar conclusion was recently obtained by Chai et al. [18] when investigating diffusion process to predict the effective mass diffusivity. To eliminate the inherent numerical error in LBGK model, the most effective solution is to adopt multiple-relaxation-time collision model [24] so that various relaxation times can be adjusted independently [9,18,25]. Thus, here we adopt the multiple-relaxation-time collision model to obtain both flow field and concentration field.

The evolution equation of density distribution function can be written as

$$f_i(\mathbf{x} + \mathbf{e}_i\delta_t, t + \delta_t) - f_i(\mathbf{x}, t) = -(\mathbf{M}^{-1}\mathbf{S})_{ij}[\mathbf{m}_j(\mathbf{x}, t) - \mathbf{m}_j^{(\text{eq})}(\mathbf{x}, t)] \tag{5}$$

where f_i is the density distribution function, $\mathbf{x}$ is the fluid parcel position, $\mathbf{e}_i$ is the discrete velocity along the ith direction, δ_t is the time-step, and $\mathbf{M}$ is a 9×9 orthogonal transformation matrix. For the two-dimensional D2Q9 lattice model, $\mathbf{e}_i$ and $\mathbf{M}$ can be found in Refs. [24] and [26]. The equilibrium moments $\mathbf{m}^{(\text{eq})}$ is given by $\mathbf{m}^{(\text{eq})} = [\rho, -2\rho + 3(j_x^2 + j_y^2), \rho - 3(j_x^2 + j_y^2), j_x, -j_x, j_y, -j_y, j_x^2 - j_y^2, j_x j_y]^{\text{T}}$, where $j_x = \rho u_x$ and $j_y = \rho u_y$ are x and y components of momentum, respectively. The relaxation matrix is given as $\mathbf{S} = \text{diag}(s_\rho, s_e, s_\epsilon, s_j, s_q, s_j, s_q, s_\nu, s_\nu)$, where the relaxation parameters are given as $s_\rho = s_j = 0$, $s_e = s_\epsilon = s_\nu = 1/\tau_f$, and $s_q = 8(2\tau_f - 1)/(8\tau_f - 1)$. The density ρ and velocity $\mathbf{u}$ are calculated as $\rho = \sum_{i=0}^{8} f_i$, $\mathbf{u} = \frac{1}{\rho}\sum_{i=0}^{8} \mathbf{e}_i f_i$.

The evolution equation of concentration distribution function can be written as

$$g_i(\mathbf{x} + \mathbf{e}_i\delta_t, t + \delta_t) - g_i(\mathbf{x}, t) = -(\mathbf{N}^{-1}\mathbf{Q})_{ij}[\mathbf{n}_j(\mathbf{x}, t) - \mathbf{n}_j^{(\text{eq})}(\mathbf{x}, t)] \tag{6}$$

where g_i is the concentration distribution function. $\mathbf{N}$ is a 5×5 orthogonal transformation matrix. For the two-dimensional D2Q5 lattice model, $\mathbf{e}_i$ and $\mathbf{N}$ can be found in Refs. [25] and [26]. The equilibrium moments $\mathbf{n}^{(\text{eq})}$ is given as $\mathbf{n}^{(\text{eq})} = [C, uC, vC, aC, 0]^{\text{T}}$, where a is a constant determined by the mass diffusivity as $a = 60D/\sqrt{3} - 4$. The relaxation matrix is given by $\mathbf{Q} = \text{diag}(0, q_D, q_D, q_e, q_\nu)$, where the relaxation parameters are given as $q_D = 3 - \sqrt{3}$ and $q_e = q_\nu = 4\sqrt{3} - 6$. The concentration C is calculated as $C = \sum_{i=0}^{4} g_i$.

2.3 Boundary Condition

2.3.1 At Solid-Fluid Interface. Heterogeneous chemical reaction at solid–fluid interfaces described by Eq. (4) is essentially

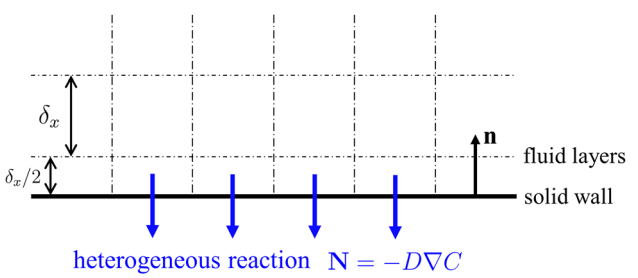

Fig. 1 Demonstration of the boundary location for heterogeneous reaction

Robin boundary condition for the concentration field, which can be written in general form as

$$b_1 C_w + b_2 \frac{\partial C_w}{\partial n} = b_3 \tag{7}$$

where $b_1 = \mathrm{Da}/L$, $b_2 = -1$, and $b_3 = \mathrm{Da}/L$. To obtain the required concentration value from the available concentration gradient at the boundary, a finite difference approximation is employed as

$$\frac{\partial C_w}{\partial n} \approx \frac{8C_w - 9C_f + C_{ff}}{3\delta_x \mathbf{n} \cdot \mathbf{e}_i} \tag{8}$$

where the subscripts f and ff denote the nearest fluid point and the next-nearest fluid point from the wall, respectively. $\mathbf{n}$ is unit vector illustrated in Fig. 1, and $\mathbf{e}_i$ is discrete velocity crosses the interface. For fluid points near flat interfaces, $\mathbf{n} \cdot \mathbf{e}_i = -1$; for fluid points near the corners, $\mathbf{n} \cdot \mathbf{e}_i = -\sqrt{2}$. Similar treatment using first-order finite difference approximation was adopted by Zhang et al. [27]. Substituting Eq. (8) into Eq. (7), the concentration value at boundary can be obtained as

$$C_w = \frac{9b_2 C_f - b_2 C_{ff} + 3b_3 \delta_x \mathbf{n} \cdot \mathbf{e}_i}{8b_2 + 3b_1 \delta_x \mathbf{n} \cdot \mathbf{e}_i} \tag{9}$$

Then, the antibounce-back boundary scheme for concentration distribution function can be adopted as [25]

$$g_{\bar{i}}(\mathbf{x}_f, t + \delta_t) = -g_i^*(\mathbf{x}_f, t) + \frac{4 + a}{10} C_w \tag{10}$$

where $g_{\bar{i}}$ is the distribution function associated with the velocity $\mathbf{e}_{\bar{i}} = -\mathbf{e}_i$.

2.3.2 At Inlet and Outlet. For simulations in a unit cell, the periodic fully developed flow and mass transfer boundary condition should be adopted in the streamwise direction [28]. The corresponding LB boundary scheme for the flow field was proposed by Zhang and Kwok [29], which modifies the outgoing density distribution function at inlet and outlet. Meanwhile, the LB boundary scheme for the concentration field employing D2Q5 lattice model is given by Yoshino and Inamuro [30].

For simulations in a disordered porous medium, one may specify prescribed pressure and concentration profiles at the inlet and outlet following Guo et al. [31] and Wang et al. [25], respectively.

2.4 Calculation of Effective Permeability and Mass Transfer Coefficient. The permeability K describes the ability of fluids flow through porous media under pressure difference ∇p. When the Reynolds number ($\mathrm{Re} = uL/\nu$) is sufficiently small, the Darcy's law states that the relationship between average velocity and pressure difference is linear. However, when the Reynolds number is finite, the Forchheimer equation indicates that the linear relationship breaks down. In this study, the Reynolds number covers both the creeping flow regime and the inertial flow regime; thus, an effective permeability K_e is calculated as $K_e = -\mu\langle \mathbf{u} \rangle / \nabla p$, where $\langle \mathbf{u} \rangle$ denotes the average velocity. At the creeping flow regime, $K_e = K$ and it only depends on the geometry of the porous media; at the inertial flow regime, the inertial of the fluids also contributes to K_e.

The mass transfer coefficient k_m quantifies the mass transfer process from bulk flow to pore surfaces as

$$k_m \delta \left(\langle C \rangle^f - \langle C \rangle^w \right) = \frac{1}{\Delta V} \int_{A_{\mathrm{int}}} \mathbf{n} \cdot D \nabla C dA \tag{11}$$

where $\delta = A_{\mathrm{int}}/\Delta V$ is the surface area per unit volume, and A_{int} is the interfacial mass transfer area. $\langle \cdot \rangle^f$ and $\langle \cdot \rangle^w$ denote the average in the fluid region and the pore surfaces, respectively. After

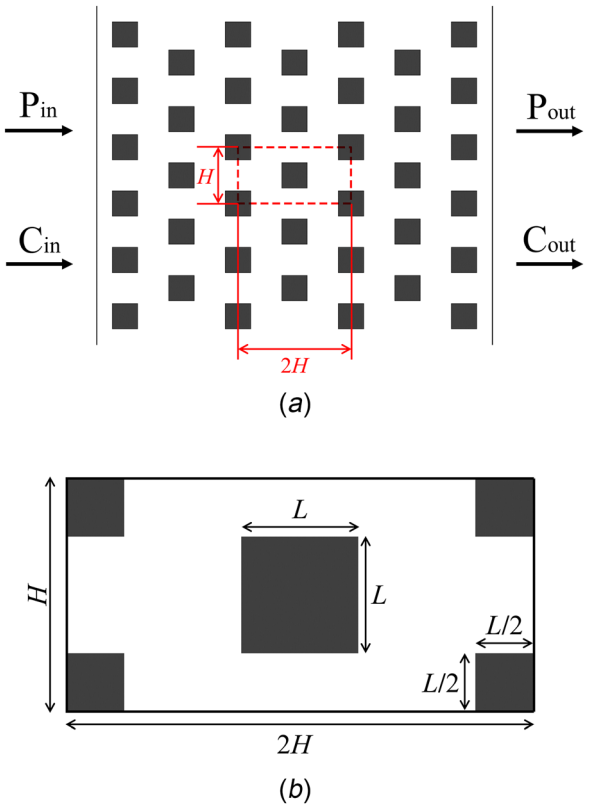

Fig. 2 Schematic drawing of a bank of square rods: (*a*) periodic structure; (*b*) a single unit cell

obtaining the concentration field information *via* pore-scale simulations, the mass transfer coefficient is calculated as

$$k_m = \frac{\sum_{i \in \mathrm{int}} \mathbf{n}_i \cdot D \nabla C_i}{A_{\mathrm{int}} \left(\langle C \rangle^f - \langle C \rangle^w \right)} \tag{12}$$

Define the Sherwood number to represent the ratio of total rate of mass transfer to the rate of diffusive mass transport as $\mathrm{Sh} = k_m/(D/L)$, where L is characteristic length. In addition, define Reynolds number and Schmidt number ($\mathrm{Sc} = \nu/D$); then Sherwood number can be expressed as a function of Reynolds number and Schmidt number as $\mathrm{Sh} = \mathrm{Sh}(\mathrm{Re}, \mathrm{Sc})$.

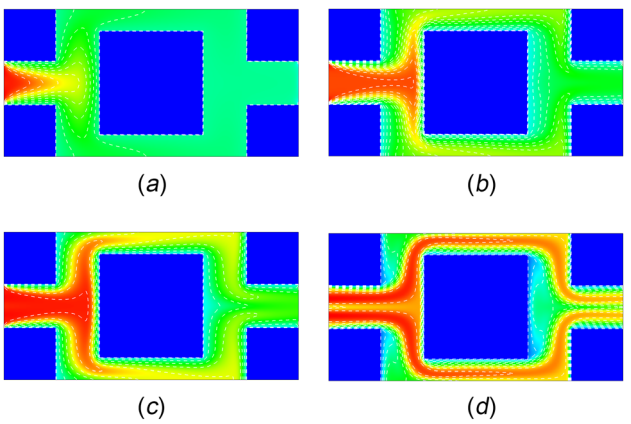

Fig. 3 Isotherms of forced convection in a bank of square rods ($\varepsilon = 0.51$): (*a*) Re = 20, Pr = 1, (*b*) Re = 112, Pr = 1, (*c*) Re = 20, Pr = 7, and (*d*) Re = 112, Pr = 7

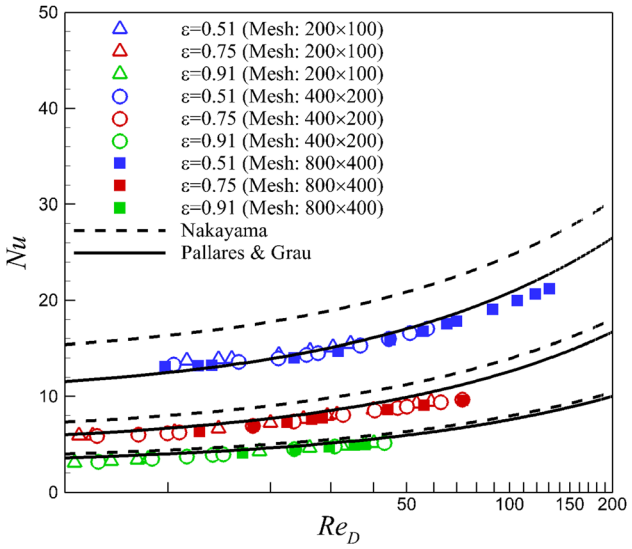

Fig. 4 Comparison of interfacial heat transfer correlations

3 Validation

A heat transfer correlation can be used in analogy to a mass transfer correlation; moreover, heat transfer correlations are readily available from literature and easier to be determined from experimental work. Thus, in the following, we assess the validity of the numerical method for simulating convective heat transfer and calculating heat transfer coefficient under constant wall temperature condition. Figure 2(*a*) shows the porous structure of a bank of square rods, and a unit cell representing the geometry is shown in Fig. 2(*b*).

Kuwahara et al. [13] proposed (later corrected by Nakayama [32]) the interfacial heat transfer coefficient as

$$\mathrm{Nu} = \left(2 + \frac{12(1-\varepsilon)}{\varepsilon}\right) + (1-\varepsilon)^{1/2}\left(\frac{u_D L}{\nu}\right)^{0.6} \mathrm{Pr}^{1/3} \tag{13}$$

where ε is porosity and $u_D = \varepsilon\langle u\rangle$ is Darcian velocity. Similarly, Pallares and Grau proposed [15] the correlation as

$$\mathrm{Nu} = \left(2 + \frac{8(1-\varepsilon)}{\varepsilon}\right) + (1-\varepsilon)^{1/2}\left(\frac{u_D L}{\nu}\right)^{0.6} \mathrm{Pr}^{1/3} \tag{14}$$

In the simulations, the periodic fully developed flow and mass transfer boundary condition (described in Sec. 2.3.2) is applied in the x direction; and the simple periodical boundary condition (i.e., the distribution functions leaving one end are the same as that entering the other end) is applied in the y direction. The Reynolds number ($\mathrm{Re}_D = u_D L/\nu$) is adjusted *via* changing the prescribed pressure difference between the inlet and the outlet. Figures 3(*a*) and 3(*b*) show the isotherms for different Reynolds numbers at $\mathrm{Pr} = 1$, which is generally in consistent with the results reported by Kuwahara et al. [13]. In addition, the isothermals at $\mathrm{Pr} = 7$ are shown in Figs. 3(*c*) and 3(*d*), which resulted in stronger convection compared with $\mathrm{Pr} = 1$.

The Nusselt number as a function of Reynolds number and porosity is shown in Fig. 4. Our LB simulation results using three different mesh sizes $N_x \times N_y = 200 \times 100$, 400×200, and 800×400 are compared with correlations presented in Eqs. (13) and (14). We can see all the results are in good agreement when the porosity is large ($\varepsilon = 0.91$). However, as the porosity decreasing, there is disparity between the correlations proposed in Eqs. (13) and (14). Our results is consistent with the correlation proposed by Pallares and Grau (i.e., Eq. (14)) when the porosity is small ($\varepsilon = 0.51$). The simulation results also demonstrate grid convergence of the numerical method.

4 Simulation Results and Discussion

4.1 Ordered Porous Medium. We first consider the coupled fluid flow, mass transfer, and heterogeneous chemical reaction in an ordered porous medium. The unit cell of the porous structure is shown in Fig. 5, where the square cylinders are either inline or staggered. In the simulations, the length of the square cylinder L can be varied to adjust the porosity ε of the unit cell. Since we have tested mesh independence for the unit cells in Sec. 3, the mesh size is chosen as 200×200 to save the computational cost without sacrificing numerical accuracy.

From the correlation between Reynolds number and effective permeability shown in Fig. 6, we can distinguish between the creeping flow regime and the inertial flow regime: the effective permeability is independent of Reynolds number at the creeping flow regime and varies with Reynolds number at the inertial flow regime. Moreover, we can see that at the same porosity, the effective permeability for square inline unit cells is larger than that for square staggered unit cells. In Fig. 7, the dimensionless mass transfer coefficients (i.e., the Sherwood numbers) are given under the same condition as that for calculating the effective permeability. One of the interesting finding is that at the creeping flow regime, the arrangement of solid obstacles in the periodic porous structure has little effect on the dimensionless mass transfer coefficient. In addition, at the inertial flow regime, the dimensionless mass transfer coefficients for square inline unit cells are smaller

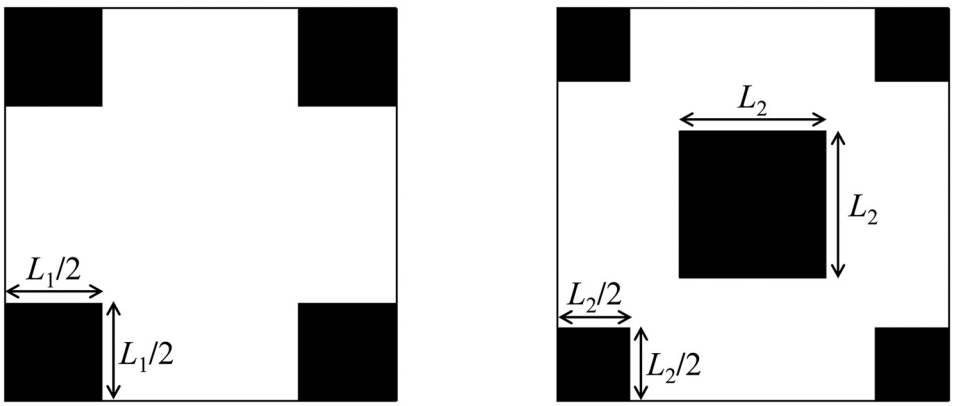

Fig. 5 Unit cells of ordered porous medium: (*a*) square inline and (*b*) square staggered

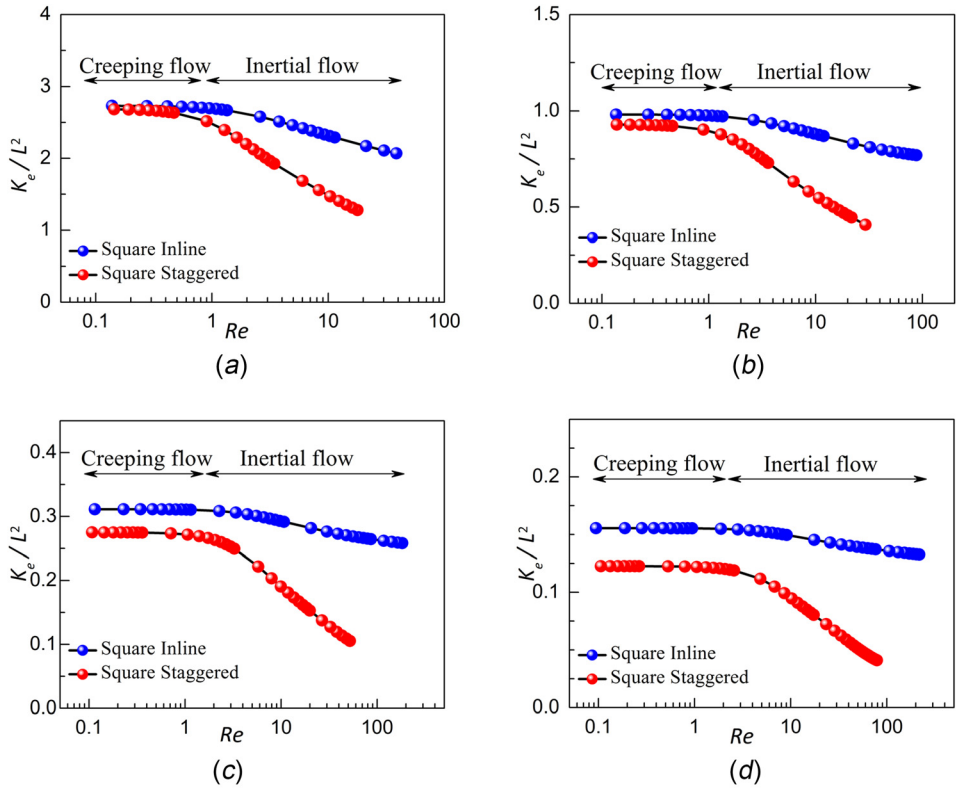

Fig. 6 Comparison of the dimensionless effective permeability (K_e/L^2) for two types of unit cells: (*a*) $\varepsilon = 0.97$, (*b*) $\varepsilon = 0.94$, (*c*), $\varepsilon = 0.88$, and (*d*) $\varepsilon = 0.83$

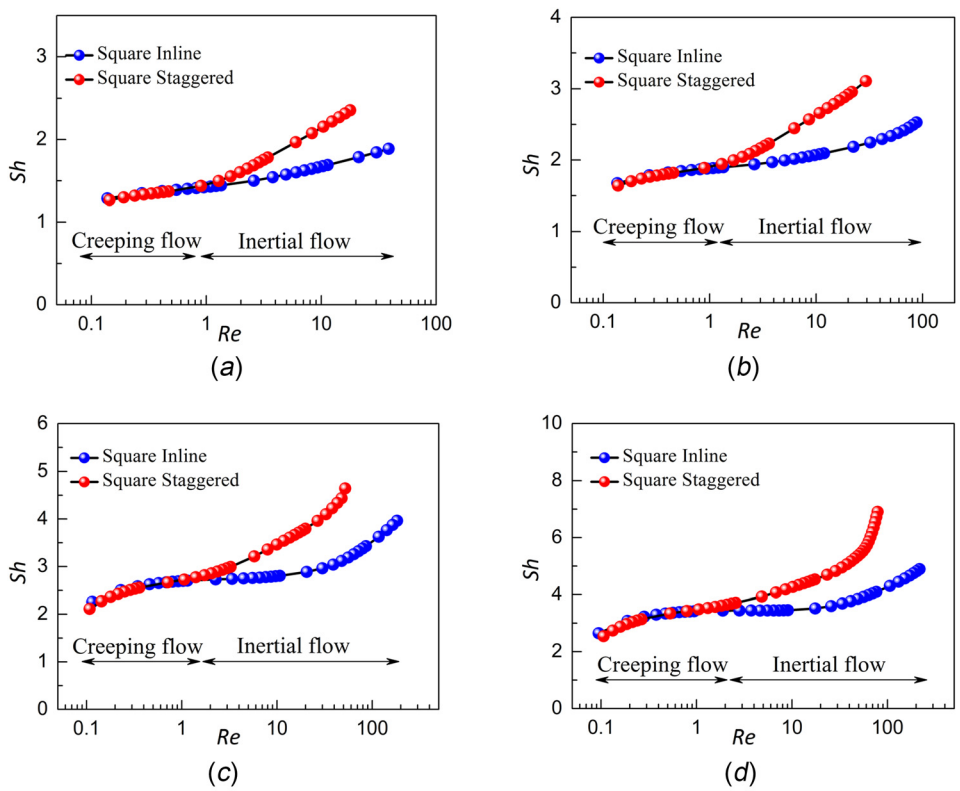

Fig. 7 Comparison of the dimensionless mass transfer coefficient (*Sh*) for two types of unit cells: (*a*) $\varepsilon = 0.97$, (*b*) $\varepsilon = 0.94$, (*c*), $\varepsilon = 0.88$, and (*d*) $\varepsilon = 0.83$

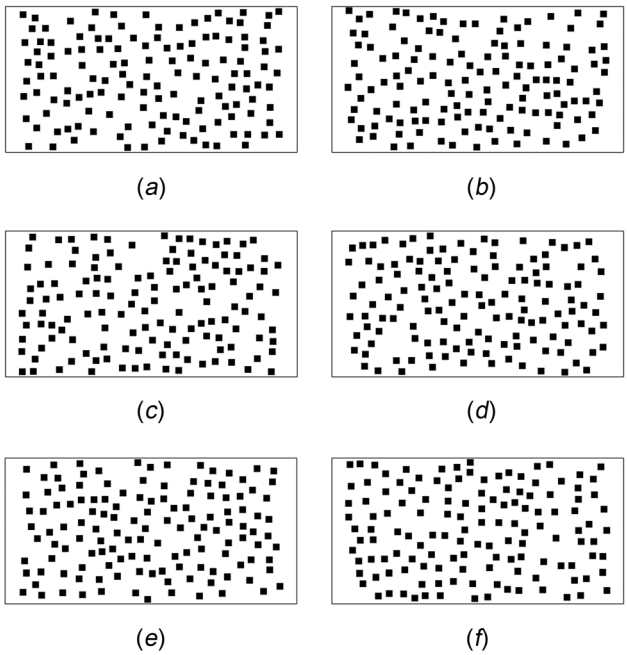

Fig. 8 Geometries of the disordered porous structure: (*a*) porous structure *A*, (*b*) porous structure *B*, (*c*) porous structure *C*, (*d*) porous structure *D*, (*e*) porous structure *E*, and (*f*) porous structure *F*

than those for square staggered unit cells at the same porosity. These results indicate that there is trade-off for choosing which types of unit cell to construct an ordered porous medium, as in practical engineering applications, particularly in fuel cells and flow batteries, one would usually pursue porous electrodes with pore geometry that can simultaneously result in large permeability and large mass transfer coefficient.

4.2 Disordered Porous Medium. We now consider a disordered porous medium consisting of randomly placed square cylinders. The computational domain is 1800×900 lattice, and the length of square cylinder is 40 lattice. The center of the square is randomly set in the computational domain, exclusively the left and the right ends of the domain to minimize the boundary effect at inlet and outlet. Any two squares are not allowed to overlap and the minimum gap between two squares is set to be 20 lattice spacing. Six sample geometries of the porous structure generated using

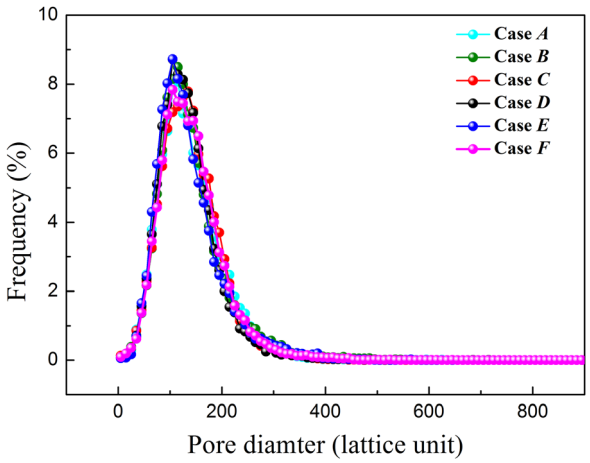

Fig. 9 Pore size distribution of the disordered porous structure

different initial seed values are shown in Figs. 8(*a*)–8(*f*), and are referred to porous structure *A*, *B*, *C*, *D*, *E*, *F* for simplicity. The prescribed pressure and concentration are set at the inlet and outlet; the periodical boundary conditions for flow field and concentration field are set in the direction perpendicular to the streamwise direction. To make the simulations more efficient, a parallel code based on open multi-processing (OpenMP) is compiled. Utilizing OpenMP acceleration, about 19×10^6 lattice updates per second can be achieved when scaled up to 24 central processing unit threads. Figure 9 gives the corresponding pore size distribution of these six disordered porous structures. The pore size distribution is calculated based on the directional average method [33,34]. At each void point, we start counting the pore length along specified directions until reaching a solid point. Then, the pore diameter is obtained by averaging the pore length in all given directions. In the present study, the eight directions same as that for the discrete velocity set $\{\mathbf{e}_1, \mathbf{e}_2, \ldots, \mathbf{e}_8\}$ were chosen. By randomly placing the square cylinders to reconstruct the porous structure, the pore size exhibits a unimodal distribution, with mean pore diameter value near three to four times the length of square cylinders. This trend is generally in agreement with pore size distribution of carbon paper, which is a widely used material for the electrode of fuel cell [1] and flow battery [2].

Figure 10 shows the streamlines (left-hand side) and concentration field (right-hand side) in the porous structure *A* under various Reynolds numbers at $\mathrm{Sc} = 1$. At very small Reynolds number (e.g., $\mathrm{Re} = 0.025$ shown in Fig. 10(*a*)), the motion of the fluid is at the creeping flow regime, and the momentum transport is dominated by the viscous force; the mass transport is dominated by diffusion, and the concentration contour is almost flat with some irregularities at a few pores. As Reynolds number increases (e.g., $\mathrm{Re} = 6.75$ shown in Fig. 10(*b*)), the inertial force begins to contribute to the transport of both momentum and mass. Some vortexes behind the cylinders appear, and the concentration contour exhibits tree-like fingers. At larger Reynolds number (e.g., $\mathrm{Re} = 45.53$ shown in Fig. 10(*c*)), the inertial effect becomes more pronounced. The streamlines are more irregular around the cylinders, and more vortexes appear behind the cylinders; the concentration fingers spread more through the porous medium, thus enhancing the mass transfer process.

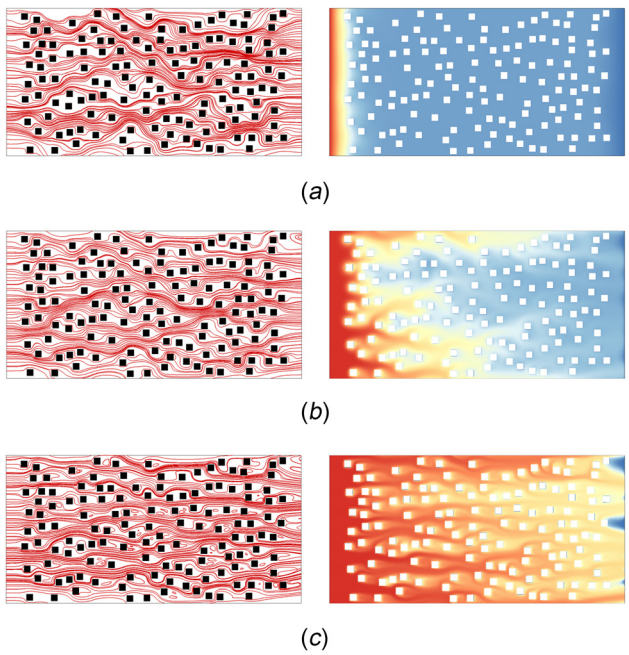

Fig. 10 Streamlines (left-hand side) and concentration field (right-hand side) in porous structure *A* from creeping flow regime to inertial flow regime: (*a*) Re = 0.025, (*b*) Re = 6.75, and (*c*) Re = 45.53

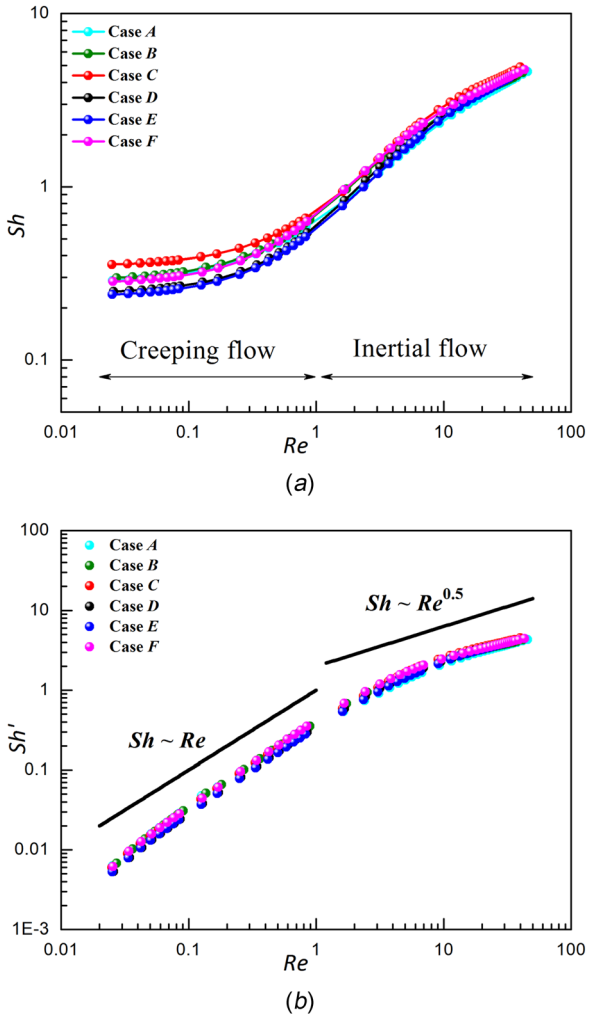

Fig. 11 Correlations between Sherwood number and Reynolds number: (*a*) $Sh = a + b\,Re^{c}Sc^{d}$ and (*b*) $Sh' = Sh - a$

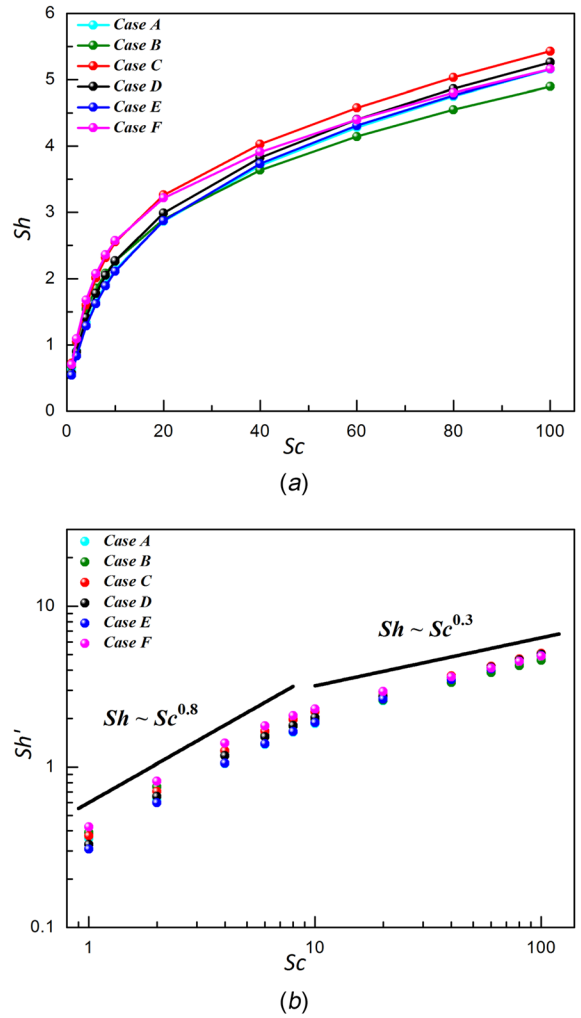

Fig. 12 Correlations between Sherwood number and Schmidt number: (*a*) $Sh = a + b\,Re^{c}Sc^{d}$ and (*b*) $Sh' = Sh - a$

Figure 11(*a*) shows the correlations between Sherwood number and Reynolds number, and Fig. 12(*a*) shows the correlations between Sherwood number and Schmidt number in the disordered porous media. The Reynolds number is in the range from creeping flow regime to inertial flow regime; the Schmidt number is in the range $1 \leq Sc \leq 100$. Here, we propose the correlation between Sherwood number and Reynolds as well as Schmidt number in the form $Sh = a + bRe^{c}Sc^{d}$, where a corresponds to the mass transfer coefficient at the diffusion limit. To determine the power index c and d, define $Sh' = Sh - a$. From Fig. 11(*b*) we can see that at the creeping flow regime, Sherwood number increases linearly with Reynolds number, namely the power index $c = 1$; at the inertial flow regime, Sherwood number and Reynolds number exhibit a one-half power law dependence, namely the power index $c = 0.5$. From Fig. 12(*b*) we can see that for $1 \leq Sc < 10$, the power index $d = 0.8$; for $10 < Sc \leq 100$, the power index $d = 0.3$.

5 Conclusion

In this work, we have presented lattice Boltzmann simulations for the mass transfer coefficient in chemically reactive flows for both ordered and disordered porous structure. The present method allows the analysis of geometrical structure effect, Reynolds number, and Schmidt number effect on the mass transfer coefficient. The main findings are summarized as follows:

(1) The ordered porous structure consists of cylinders in a staggered arrangement exhibits a larger mass transfer coefficient than cylinders in a line arrangement do, while the opposite relation holds for effective permeability. This indicates the trade-off for choosing the geometrical structure of an ordered porous medium to simultaneously maximize flow and mass transfer.

(2) The disordered porous structures consists of randomly placed cylinders, the correlation between Sherwood number and Reynolds number can be divided into two parts: at the creeping flow regime, the Sherwood number increases linearly with Reynolds number, namely $Sh \propto Re$; at the inertial flow regime, the Sherwood number and Reynolds number exhibit a one-half power law dependence, namely $Sh \propto Re^{0.5}$. Meanwhile, for Schmidt number $1 \leq Sc < 10$, $Sh \propto Sc^{0.8}$; for Schmidt number $10 < Sc \leq 100$, $Sh \propto Sc^{0.3}$.

Funding Data

- Research Grants Council, University Grants Committee (Grant No. 623313).

Nomenclature

c, C = concentration (mol/m^3)
D = mass diffusivity (m^2/s)
Da = Damköhler number
f, g = distribution function
k_m = mass transfer coefficient

K_e = effective permeability
L = characteristic length (m)
Nu = Nusselt number
p = pressure (Pa)
Pr = Prandtl number
Re = Reynolds number
Sc = Schmidt number
Sh = Sherwood number
t = time (s)
$\mathbf{u}$ = velocity vector (m/s)
x, y = coordinates (m)
ε = porosity
μ = dynamic viscosity (Pa·s)
ν = kinematic viscosity (m^2/s)
ρ = density (Kg/m^3)

Subscripts or Superscripts

eq = equilibrium
int = interface
w = wall

References

[1] Zhao, T. S., Xu, C., Chen, R., and Yang, W. W., 2009, "Mass Transport Phenomena in Direct Methanol Fuel Cells," Prog. Energy Combust. Sci., **35**(3), pp. 275–292.
[2] Xu, Q., and Zhao, T., 2015, "Fundamental Models for Flow Batteries," Prog. Energy Combust. Sci., **49**, pp. 40–58.
[3] Whitaker, S., 1999, *The Method of Volume Averaging*, Vol. 13, Springer Science & Business Media, Dordrecht, The Netherlands.
[4] Davit, Y., Bell, C. G., Byrne, H. M., Chapman, L. A., Kimpton, L. S., Lang, G. E., Leonard, K. H., Oliver, J. M., Pearson, N. C., Shipley, R. J., Waters, S. L., Whiteley, J. P., Wood, B. D., and Quintard, M., 2013, "Homogenization Via Formal Multiscale Asymptotics and Volume Averaging: How Do the Two Techniques Compare?," Adv. Water Resour., **62**(Pt. B), pp. 178–206.
[5] Xu, Q., and Zhao, T., 2013, "Determination of the Mass-Transport Properties of Vanadium Ions Through the Porous Electrodes of Vanadium Redox Flow Batteries," Phys. Chem. Chem. Phys., **15**(26), pp. 10841–10848.
[6] Rashapov, R. R., and Gostick, J. T., 2016, "In-Plane Effective Diffusivity in PEMFC Gas Diffusion Layers," Transp. Porous Media, **115**(3), pp. 411–433.
[7] Mattila, K., Puurtinen, T., Hyväluoma, J., Surmas, R., Myllys, M., Turpeinen, T., Robertsen, F., Westerholm, J., and Timonen, J., 2016, "A Prospect for Computing in Porous Materials Research: Very Large Fluid Flow Simulations," J. Comput. Sci., **12**, pp. 62–76.
[8] Xu, A., Shyy, W., and Zhao, T., 2017, "Lattice Boltzmann Modeling of Transport Phenomena in Fuel Cells and Flow Batteries," Acta Mech. Sin., **33**(3), pp. 555–574.
[9] Pan, C., Luo, L.-S., and Miller, C. T., 2006, "An Evaluation of Lattice Boltzmann Schemes for Porous Medium Flow Simulation," Comput. Fluids, **35**(8), pp. 898–909.
[10] Chai, Z., Shi, B., Lu, J., and Guo, Z., 2010, "Non-Darcy Flow in Disordered Porous Media: A Lattice Boltzmann Study," Comput. Fluids, **39**(10), pp. 2069–2077.
[11] Wang, M., Wang, J., Pan, N., and Chen, S., 2007, "Mesoscopic Predictions of the Effective Thermal Conductivity for Microscale Random Porous Media," Phys. Rev. E, **75**(3), p. 036702.
[12] Yao, Y., Wu, H., and Liu, Z., 2017, "Pore Scale Investigation of Heat Conduction of High Porosity Open-Cell Metal Foam/Paraffin Composite," ASME J. Heat Transfer, **139**(9), p. 091302.
[13] Kuwahara, F., Shirota, M., and Nakayama, A., 2001, "A Numerical Study of Interfacial Convective Heat Transfer Coefficient in Two-Energy Equation Model for Convection in Porous Media," Int. J. Heat Mass Transfer, **44**(6), pp. 1153–1159.
[14] Saito, M. B., and De Lemos, M. J., 2006, "A Correlation for Interfacial Heat Transfer Coefficient for Turbulent Flow Over an Array of Square Rods," ASME J. Heat Transfer, **128**(5), pp. 444–452.
[15] Pallares, J., and Grau, F., 2010, "A Modification of a Nusselt Number Correlation for Forced Convection in Porous Media," Int. Commun. Heat Mass Transfer, **37**(9), pp. 1187–1190.
[16] Torabi, M., Torabi, M., and Peterson, G., 2016, "Heat Transfer and Entropy Generation Analyses of Forced Convection Through Porous Media Using Pore Scale Modeling," ASME J. Heat Transfer, **139**(1), p. 012601.
[17] Jeong, N., Choi, D. H., and Lin, C.-L., 2008, "Estimation of Thermal and Mass Diffusivity in a Porous Medium of Complex Structure Using a Lattice Boltzmann Method," Int. J. Heat Mass Transfer, **51**(15), pp. 3913–3923.
[18] Chai, Z., Huang, C., Shi, B., and Guo, Z., 2016, "A Comparative Study on the Lattice Boltzmann Models for Predicting Effective Diffusivity of Porous Media," Int. J. Heat Mass Transfer, **98**, pp. 687–696.
[19] Grucelski, A., and Pozorski, J., 2015, "Lattice Boltzmann Simulations of Heat Transfer in Flow Past a Cylinder and in Simple Porous Media," Int. J. Heat Mass Transfer, **86**, pp. 139–148.
[20] Gamrat, G., Favre-Marinet, M., and Le Person, S., 2008, "Numerical Study of Heat Transfer Over Banks of Rods in Small Reynolds Number Cross-Flow," Int. J. Heat Mass Transfer, **51**(3), pp. 853–864.
[21] Sheikholeslami, M., and Shehzad, S., 2017, "Magnetohydrodynamic Nanofluid Convection in a Porous Enclosure Considering Heat Flux Boundary Condition," Int. J. Heat Mass Transfer, **106**, pp. 1261–1269.
[22] Xu, A., Shi, L., and Zhao, T., 2018, "Lattice Boltzmann Simulation of Shear Viscosity of Suspensions Containing Porous Particles," Int. J. Heat Mass Transfer, **116**, pp. 969–976.
[23] Qian, Y., d'Humières, D., and Lallemand, P., 1992, "Lattice BGK Models for Navier-Stokes Equation," EPL (Europhys. Lett.), **17**(6), pp. 479–572.
[24] Lallemand, P., and Luo, L.-S., 2000, "Theory of the Lattice Boltzmann Method: Dispersion, Dissipation, Isotropy, Galilean Invariance, and Stability," Phys. Rev. E, **61**(6), p. 6546.
[25] Wang, J., Wang, D., Lallemand, P., and Luo, L.-S., 2013, "Lattice Boltzmann Simulations of Thermal Convective Flows in Two Dimensions," Comput. Math. Appl., **65**(2), pp. 262–286.
[26] Xu, A., Shi, L., and Zhao, T., 2017, "Accelerated Lattice Boltzmann Simulation Using GPU and OpenACC With Data Management," Int. J. Heat Mass Transfer, **109**, pp. 577–588.
[27] Zhang, T., Shi, B., Guo, Z., Chai, Z., and Lu, J., 2012, "General Bounce-Back Scheme for Concentration Boundary Condition in the Lattice-Boltzmann Method," Phys. Rev. E, **85**(1), p. 016701.
[28] Patankar, S., Liu, C., and Sparrow, E., 1977, "Fully Developed Flow and Heat Transfer in Ducts Having Streamwise-Periodic Variations of Cross-Sectional Area," ASME J. Heat Transfer, **99**(2), pp. 180–186.
[29] Zhang, J., and Kwok, D. Y., 2006, "Pressure Boundary Condition of the Lattice Boltzmann Method for Fully Developed Periodic Flows," Phys. Rev. E, **73**(4), p. 047702.
[30] Yoshino, M., and Inamuro, T., 2003, "Lattice Boltzmann Simulations for Flow and Heat/Mass Transfer Problems in a Three-Dimensional Porous Structure," Int. J. Numer. Methods Fluids, **43**(2), pp. 183–198.
[31] Guo, Z.-L., Zheng, C.-G., and Shi, B.-C., 2002, "Non-Equilibrium Extrapolation Method for Velocity and Pressure Boundary Conditions in the Lattice Boltzmann Method," Chin. Phys., **11**(4). pp. 366–374.
[32] Nakayama, A., 2014, "A Note on the Confusion Associated With the Interfacial Heat Transfer Coefficient for Forced Convection in Porous Media," Int. J. Heat Mass Transfer, **79**, pp. 1–2.
[33] Lange, K. J., Sui, P.-C., and Djilali, N., 2010, "Pore Scale Simulation of Transport and Electrochemical Reactions in Reconstructed PEMFC Catalyst Layers," J. Electrochem. Soc., **157**(10), pp. B1434–B1442.
[34] Chen, L., Wu, G., Holby, E. F., Zelenay, P., Tao, W.-Q., and Kang, Q., 2015, "Lattice Boltzmann Pore-Scale Investigation of Coupled Physical-Electrochemical Processes in C/Pt and Non-Precious Metal Cathode Catalyst Layers in Proton Exchange Membrane Fuel Cells," Electrochimica Acta, **158**, pp. 175–186.